ADVANCED FUNCTIONAL MATERIALS
www.afm-journal.de

Grain-Boundary-Rich Noble Metal Nanoparticle Assemblies: Synthesis, Characterization, and Reactivity

Xin Geng, Shuwei Li, Jaeyoung Heo, Yi Peng, Wenhui Hu, Yanchao Liu, Jier Huang, Yang Ren, Dongsheng Li, Liang Zhang,* and Long Luo**

Here, a comprehensive study on the synthesis, characterization, and reactivity of grain-boundary (GB)-rich noble metal nanoparticle (NP) assemblies is presented. A facile and scalable synthesis of Pt, Pd, Au, Ag, and Rh NP assemblies is developed, in which NPs are predominantly connected via Σ3 (111) twin GBs, forming a network. Driven by water electrolysis, the random collisions and oriented attachment of colloidal NPs in solution lead to the formation of Σ3 (111) twin boundaries and some highly mismatched GBs. This synthetic method also provides convenient control over the GB density without altering the crystallite size or GB type by varying the NP collision frequency. The structural characterization reveals the presence of localized tensile strain at the GB sites. The ultrahigh activity of GB-rich Pt NP assembly toward catalytic hydrogen oxidation in air is demonstrated, enabling room-temperature catalytic hydrogen sensing for the first time. Finally, density functional theory calculations reveal that the strained Σ3(111) twin boundary facilitates oxygen dissociation, drastically enhancing the hydrogen oxidation rate via the dissociative pathway. This reported large-scale synthesis of the Σ3 (111) twin GB-rich structures enables the development of a broad range of high-performance GB-rich catalysts.

1. Introduction

Grain boundaries (GBs) have been previously used extensively to control mechanical strength, plasticity, and conductivity,[1] and recently, the interest in GBs has extended to their catalytic properties. For example, Kanan and co-workers found that the GB sites of Au and Cu were responsible for the improved CO_2-to-CO and CO-to-fuels electrocatalytic activity.[2–6] Matteo and co-workers discovered that the Pd twin boundaries enhanced the catalytic methane oxidation activity and lowered the initiation temperature for this reaction.[7] Du and co-workers found that GB-rich Ru and Ag nanoparticles (NPs) were highly active for oxygen evolution reaction and hydrogen evolution reaction, respectively.[8,9]

Catalytic GB-rich materials have been prepared using various methods, including reducing metal oxide,[10,11] stream treatment,[7] vapor deposition,[3,5] laser ablation,[8,9] controlled electrodeposition with additives,[12] polyol,[10,11] and nanocrystal-coining process.[12] Despite these advancements, it is still difficult to control the GB type and density during material synthesis, making it challenging to establish reliable structure-activity relationships for GB-rich catalytic nanomaterials.

Thermal post-treatment is currently the most common method used to vary the GB density for establishing the quantitative correlation between GBs and catalytic activity.[3,5] During thermal annealing, the GB density decreases. However, such GB density decrease is often accompanied by other structural changes such as grain size increase, causing complexities in interpreting the GB density–activity correlations.

Here, we report a facile and scalable synthesis of GB-rich noble metal NP assemblies (including Pt, Pd, Au, Ag, and Rh) from their colloidal NPs. We utilize the electrogenerated local

X. Geng, Y. Peng, L. Luo
Department of Chemistry
Wayne State University
Detroit, MI 48202, USA
E-mail: long.luo@wayne.edu

S. Li, L. Zhang
Center for Combustion Energy
School of Vehicle and Mobility
State Key Laboratory of Automotive Safety and Energy
Tsinghua University
Beijing 100084, China
E-mail: zhangbright@tsinghua.edu.cn

The ORCID identification number(s) for the author(s) of this article can be found under https://doi.org/10.1002/adfm.202204169.

DOI: 10.1002/adfm.202204169

J. Heo, D. Li
Physical and Computational Sciences Directorate
Pacific Northwest National Laboratory
Richland, WA 99352, USA
E-mail: dongsheng.li2@pnnl.gov

W. Hu, J. Huang
Department of Chemistry
Marquette University
Milwaukee, WI 53201, United States

Y. Liu
Department of Industrial and Systems Engineering
Wayne State University
Detroit, MI 48202, USA

Y. Ren
Department of Physics
City University of Hong Kong
Hong Kong SAR, China

high pH at the cathode to destabilize the NPs and the convective flow to promote their collisions and attachments in solution, forming the Σ3 (111) and Σ11 (113) twin boundaries and some disordered grain boundaries, among which Σ3 is most stable[13] and dominates in the assemblies. The high thermodynamic stability of Σ3 twin boundaries in NP assemblies is also essential for catalytic applications.[7] The crystallite size is unchanged during the assembly process. The GB density can be easily modulated by controlling the collision frequency. The structural characterization using X-ray absorption spectroscopy (XAS), high-resolution x-ray diffraction (HR-XRD), and high-resolution transmission electron microscopy (HR-TEM) reveals the GB sites are highly strained, and this strain has more tensile character than compressive.

Furthermore, we demonstrate the ultrahigh activity of Pt NP assembly toward catalytic hydrogen oxidation in air (≈400-fold higher than commercial Pt catalysts), enabling catalytic hydrogen sensing even at room temperature. Catalytic sensors detect H_2 based on the exothermic oxidation reaction of H_2 with air on a catalyst surface (typically, Pt), which generates heat to change the electrical resistance of the catalyst for determining the H_2 concentration. However, due to the low activity of Pt catalysts in conventional catalytic H_2 sensors, a high operating temperature of ≈500 °C is often required (achieved by external heating), causing high power consumption (≈0.5–3.0 W) and severe cross-sensitivity to other combustible gases, such as hydrocarbons, CO, etc.[14–17] In addition, the performance of catalytic H_2 sensors is also affected following exposure to "poisoning gases", such as H_2S and SO_2 (even at ppm level), which adsorb onto the Pt catalyst more strongly than H_2, thereby reducing the number of sites available to catalyze H_2 oxidation.[17] To overcome the limitations of catalytic H_2 sensors, prior efforts were focused on the miniaturization of the sensors, resulting in lower power consumption, and faster response times.[18–23] However, the cross-sensitivity to combustible gases and susceptibility to catalyst poisoning is still not addressed. The room-temperature catalytic H_2 sensor built on our Pt NP assembly fully addresses the cross-sensitivity problem.

Finally, we found the linear correlation between the GB density and catalytic activity, confirming that the GB sites are responsible for the high activity. Density functional theory calculations reveal that the strained Σ3(111) twin boundary facilitates oxygen dissociation, drastically enhancing the hydrogen oxidation rate via the dissociative pathway.

2. Results and Discussion

2.1. Electrosynthesis of GB-Rich Pt NP Assemblies

As illustrated in **Figure 1**a, the GB-rich Pt NP assembly was synthesized by conducting water electrolysis in an unbuffered, high-concentration (≈1.7×10^{-6} M) colloidal Pt NP solution. The water reduction at the cathode created a local high pH of ≈14 to assist the complete removal of citrate capping agents from the Pt NP surface (Figure S1, Supporting Information). Meanwhile, gas bubbles generated during water electrolysis promote the random collisions of the destabilized Pt NPs after ligand removal, driving individual NPs to assemble into NP clusters, chains, networks, and eventually a macroscopic (sub-centimeter-sized) solid at the cathode (Figure 1b,c; Figure S2, Supporting Information). The nanoscale chain-like morphology in the Pt NP assembly is characteristic of a diffusion-limited cluster aggregation process (Figure S3, Supporting Information).[24,25] Scanning transmission electron microscopic (STEM) images of Pt NPs and Pt NP assembly show no significant crystallite size change after the water-electrolysis-driven NP assembly (Pt NPs: 3.6 ± 0.5 nm and Pt NP assembly: 3.8 ± 0.7 nm, Figure 1d; Figure S4, Supporting Information). HR-TEM and STEM images revealed that individual Pt NP building blocks in the Pt NP assembly were primarily connected by GBs. The representative GBs identified in the Pt NP assembly are Σ3 (111) twin boundaries, where two NPs share the low energy {111} planes (e.g., NP1 and NP2 in Figure 1e).[26,27]

From randomly selected 58 GBs that are at the [110] viewing direction, we identified 53 Σ3 GBs, three Σ11 GBs (Figure S5, Supporting Information), two mismatched (111)/(200) GBs (e.g., the GB between the {111} plane of NP4 and the {200} plane of NP5 in Figure 1e), indicating the dominance of Σ3 GBs in Pt NP assembly. The dominance of Σ3 GBs suggests that Pt NPs most likely undergo oriented attachment (OA), during which spontaneous self-organization of adjacent particles is involved so that they share a common crystallographic orientation ({111} in our case), followed by the joining of these particles at a planar interface.[28,29] It is also worth noting that an interface-free structure can also form when two NPs are perfectly aligned along the {111} planes (e.g., NP3 and NP4 in Figure 1e).

The robust and practical nature of our electrosynthetic method was demonstrated by the gram-scale preparation of GB-rich Pt NP assembly. By simply scaling up the Pt NP solution volume to 1 L and increasing the electrode size, we successfully synthesized ≈1 g of GB-rich Pt NP assembly (Figure 1f,g). The synthesized material shows a similar morphology of the 3D NP network as that synthesized at the milligram scale (Figure S6, Supporting Information).

2.2. Structural Characterization

Next, we carried out a detailed structural characterization of Pt NPs and their GB-rich assembly using XAS, HR-XRD, and HR-TEM. The XAS result in Figure S7 (Supporting Information) shows that Pt NPs and their assembly have similar Pt-Pt bond lengths (Pt NPs: 0.277 ± 0.002 nm; Pt NP assembly: 0.278 ± 0.002 nm), indicating no global lattice expansion or shrinkage, but different Debye–Waller factors (Pt NPs: 8.2 ± 0.1 and Pt NP assembly:10 ± 0.1, unit: 10^{-3} Å^2), meaning that Pt NP assembly has higher local structural disorder than Pt NPs.[30] The HR-XRD spectra in **Figure 2**a present similar structural information. The XRD peaks of Pt NP assembly show no position changes but noticeable broadening relative to Pt NPs (Figure 2a,b; Figure S8, Supporting Information). Microstrain, crystallite size, and instrumental errors together determine XRD peak broadening.[31–33] Given the same instrumental errors and similar crystallite sizes of Pt NPs and Pt NP assembly (Figure 1d), the result in Figure 2a suggests the presence of increased microstrain in the Pt NP assembly. More interestingly, the XRD peak broadening for Pt NP assembly is anisotropic and

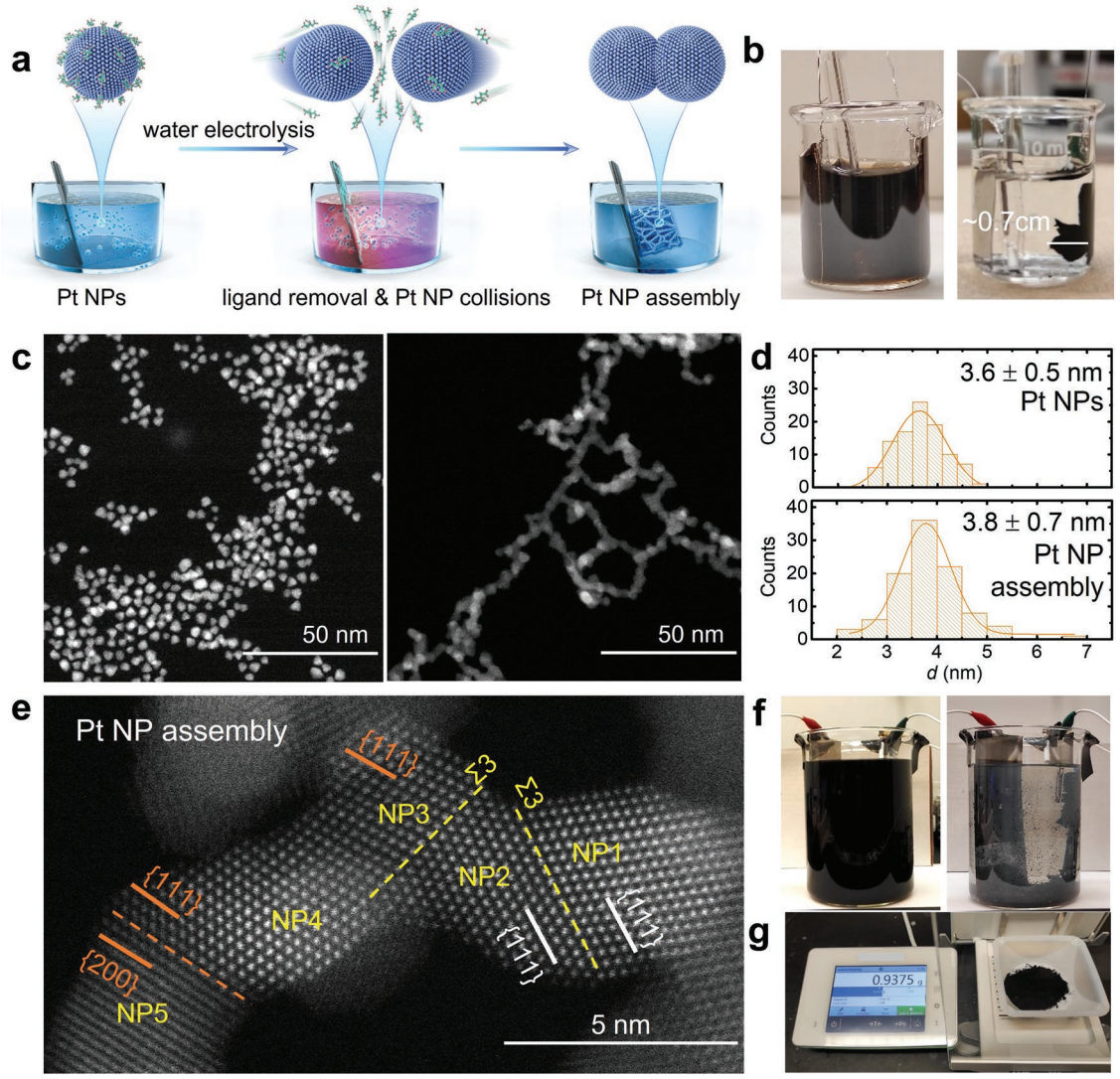

Figure 1. Electrosynthesis of GB-rich Pt NP assembly from colloidal Pt NPs. a) Schematic drawing of the NP assembly process driven by NP collisions under water electrolysis conditions that results in the formation of a macroscopic GB-rich Pt NP assembly at the cathode. The local high pH near the cathode assists the citrate ligand removal from the Pt NP surface, and the electrogenerated gas bubbles promote the Pt NP collisions in solution. b–d) Photographs, STEM images, and crystallite size distributions of Pt NPs and Pt NP assembly. The size distribution was obtained by analyzing ≈100 NPs or crystallites. e) HR-STEM image of the GBs between the Pt NP building blocks in Pt NP assembly. f) Photographs of the gram-scale synthesis setup. g) Approximately 1 g of synthesized Pt NP assembly powder after critical point drying.

asymmetric: i) the peak broadening is more significant for the (111) peak (≈17%) than others (e.g., 10% for (200) and 4% for (311) in Figure 2b) and ii) the (111) peak of Pt NP assembly was broadened by ≈18% on the left side but ≈10% on the right side at half maximum, indicating the [111] direction is highly strained, and this strain has more tensile character than compressive.[32]

We analyzed the HR-TEM image of an exemplary Σ3 (111) GB (Figure 2c,d; Figure S9, Supporting Information) and found an expansion (≈0.1 nm) (i.e., tensile strain) of lattice spacing between {111} planes (d_{111}) across the GB, relative to d_{111} of a single Pt NP (Figure 2e). In contrast, there was no apparent expansion or contraction for d_{200} (Figure 2f) comparing the single Pt NP and Pt NP assembly. These results are consistent with the XRD result that d_{111} is more strained than d_{200} in Pt NP assembly (Figure 2a,b) and demonstrate Σ3 GB-induced tensile strain. Based on the analysis of HR-TEM images, we also obtained the statistics of the *d*-spacing values for {111} and {200} planes. The *d*-spacing of Pt NP assembly exhibited a broader (≈20%) distribution than Pt NPs, but their averaged spacings for {111} and {200} are almost the same: 0.226/0.225 and 0.195/0.196 nm, respectively (Figure 2g; Figure S10, Supporting Information), in good agreement with the XAS and HR-XRD results: Pt NP assembly has no global lattice strain but higher local structural disorder or microstrain, compared to Pt NPs.

2.3. Synthesis Scope

Encouraged by the successful preparation of the GB-rich Pt NP assembly, we further explored the scope of our synthetic

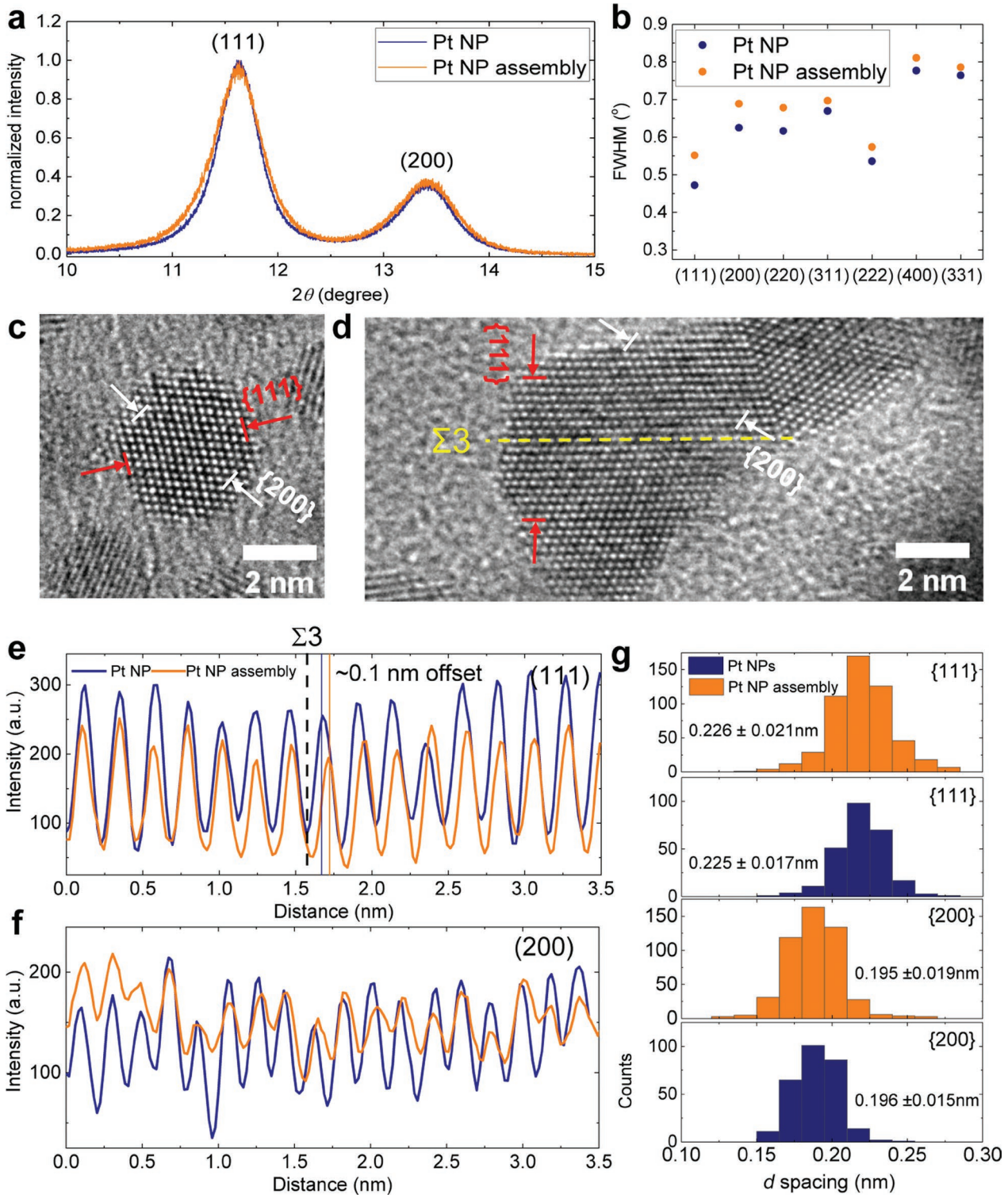

Figure 2. Structural characterization of the Σ3 (111) twin GBs in Pt NP assembly. a) High-resolution XRD spectra of Pt NPs and Pt NP assembly showing the (111) and (200) diffraction peaks. b) Full width at half maximum (FWHM) of the XRD peaks for Pt NPs and Pt NP assembly. c,d) HRTEM images of (c) Pt NP and (d) Pt NP assembly near a Σ3 (111) twin GB. e,f) The integrated pixel intensities of Pt NP and Pt NP assembly along e) {111} and f) {200} spacing directions. The peaks and valleys represent the atoms and gaps, respectively. The spacings of Pt {111} and Pt {200} planes were averaged over three atomic layers for high accuracy as labeled in (c) and (d). The lattice expansion at the Σ3 GB along the {111} direction leads to an offset between the intensity profiles of Pt NP and Pt NP assembly in (e). g) Statistics of *d* spacings for the {111} and {200} planes, analyzed under the TEM pixel size of 0.0149 nm, shows Pt NP assembly has a similar mean value as Pt NP assembly but a broader distribution of *d* spacings than NPs (for {111}, standard deviation: 0.021 vs 0.017 nm; for {200}, standard deviation: 0.019 vs 0.015 nm). The *d*-spacing distributions were obtained by analyzing ≈300 *d*-spacing values.

method. First, we tested Pt NPs with other ligands, including β-alanine, β-cyclodextrin (β-CD), sodium deoxycholate (NaDC), and polyvinylpyrrolidone (PVP). For β-alanine-and β-CD-capped Pt NPs, a cathodic potential of −2 V was sufficient to drive the self-assembly of Pt NPs into a network, like the citrate-capped Pt NPs. However, a high potential of −6 V was necessary for NaDC and PVP-capped NPs, possibly because the strong interactions of NaDC and PVP with the Pt NP surface require a higher local pH to remove the ligands. All synthesized Pt NP assemblies show the presence of Σ3 (111) twin GBs (**Figure 3**a–d), regardless of the ligand type.

Then, we moved on to other noble metals, including Pd, Au, Ag, and Rh. Similarly, the observed GBs in Pd, Au, and Rh NP assemblies were dominantly Σ3 (111) twin GBs (Figure 3e–j). Like Pt, the Σ3 (111) twin GBs of these noble metals also form via oriented attachments because 1) the oriented attachment via {111} facets is typically thermodynamically favored during particle attachments,[13,26] and 2) the majority of the exposed surface facets for face-centered cubic metals are {111} upon which most collisions occur.[26,28] However, multiply twinned structures were observed for Au NPs and citrate-capped Pd NPs, but not for Pt or Rh. Multiply twinned structures have been previously reported to form by creating and decomposing high-energy grain boundaries during multiple OA events, which is favorable for metals with low twin-fault energies such as Pd (106 mJ m^{-2}) and Au (26 mJ m^{-2}) in contrast to Pt (161 mJ m^{-2}) and Rh (145 mJ m^{-2}).[26,34,35] After replacing citrate ligands on Pd NPs with β-CD, we did not observe the formation of fivefold twins (Figure 3f), possibly because β-CD interacts more strongly with Pd than citrate. For Ag, we found the presence of some Σ3 (111) twin GBs and numerous stacking faults, i.e., fringes that are parallel to the twin boundary (Figure S11, Supporting Information). The presence of stacking faults is likely because i) the intrinsic stacking fault energy of Ag is the lowest among common face-centered-cubic metals;[35] and ii) the relatively large particle size (≈15 nm) of Ag NPs requires the large lattice strain relaxation, causing the formation of stacking faults.[36,37] Photographs of the synthesized NP assemblies from various NPs were provided in Figure S12 (Supporting Information).

The crystallite sizes of the NPs and their corresponding assemblies were analyzed using TEM and XRD. The XRD spectra in Figure 3k show that the peak widths of the NPs and their corresponding assemblies were similar in most cases, indicating that the average crystallite size was not noticeably altered during the assembly process. The only exception is the citrate-capped Au NPs, where the peak becomes narrower after assembly, meaning significant crystallite size growth. Quantitatively, Figure 3m plots the crystallite sizes calculated from the {111} diffraction peak widths using the Scherrer equation,[38,39] in excellent agreement with the crystallite sizes obtained from TEM sizing in Figure 3l.

2.4. NP Assembly Mechanism

As mentioned above, NP assemblies formed at the cathode side, suggesting that the local environment created by the electroreduction of water is essential to the assembly of NPs. During water reduction, H_2 gas bubbles are generated, and the local pH soars to 14 (Figure S1, Supporting Information). As alluded above, a possible mechanism for the water-electrolysis-driven Pt NP assembly is that the local high pH at the cathode assists the removal of the citrate capping agent. At the same time, the bubble-induced convective flow promotes the random collisions of the destabilized Pt NPs after ligand removal, driving the assembly of NPs into a network via OA.

To test this proposed mechanism, we evaluated the effects of high pH, H_2, and fluidic flow on the NP assembly individually and combined (Figure S13, Supporting Information). Specifically, we added NaOH to adjust the solution pH, stirred the solution or bubbled air to introduce fluidic flow, and dissolved H_2 into the NP solution to provide H_2. The synthetic conditions without fluidic flow failed to assemble NPs into an NP network (Figure S13d,f, Supporting Information), indicating the importance of fluidic flow. However, unexpectedly, pH 14 combined with the convective flow failed as well (Figure S13i, j, Supporting Information). Instead, we observed dense NP aggregates, which is the structural feature of a reaction-limited aggregation process (Figure S3, Supporting Information),[24,25] suggesting that this condition does not favor the GB and network formation through particle attachments. Most sodium citrate ligands were removed from the Pt NPs under high pH (Figure S1, Supporting Information), however, high pH alone is not capable of causing NP assembly, possibly because after replacing citrate ligands on the NP surface, OH^- still hinders the NP attachments due to the electrostatic repulsion between NPs from the negative charge of OH^-.

Interestingly, Pt NP assemblies were formed by stirring the Pt NP solution presaturated with dissolved H_2 (Figure S13g, Supporting Information) or simply bubbling the Pt NP solution with H_2 gas (Figure S13h, Supporting Information). H_2 molecules are known to spontaneously dissociate to form weakly adsorbed H atoms on Pt surface in the aqueous phase (the adsorption Gibbs free energy change, $\Delta G_a = \approx -2$ kJ mol^{-1}),[40] which is thermodynamically feasible to partially displace citrate ligands (ΔG_a for citrate is on the order of −10 kJ mol^{-1}).[41] We confirmed the displacement of citrates by adsorbed H using the ζ-potential measurements, which showed that the ζ-potential of Pt NPs dropped from −48 to −41 mV after purging the Pt NP solution with H_2 gas. A possible reason for the more facile NP attachment in the presence of H_2 than high pH is that adsorbed H is a neutral capping agent, thereby effectively reducing electrostatic repulsion and steric hindrance between NPs during assembly.[42] For i) Pt NPs capped with strongly interacting ligands such as PVP and ii) Au NPs having weak interactions with H_2, bubbling H_2 gas alone was unable to initiate the assembly process, and a high solution pH was required (Figures S14–S16, Supporting Information), suggesting OH^- is necessary for removing strong interacting ligands.

Taking all evidence together, the assembly of NPs should proceed via the following mechanism (Figure S13m, Supporting Information): both OH^- and H_2 participate in the ligand removal from the NP surface, reducing the steric and electrostatic repulsions between NPs. Meanwhile, bubble-induced convective flow promotes the random collisions of destabilized NPs in solution. When the colliding NPs share a common crystallographic orientation ({111} in most cases),

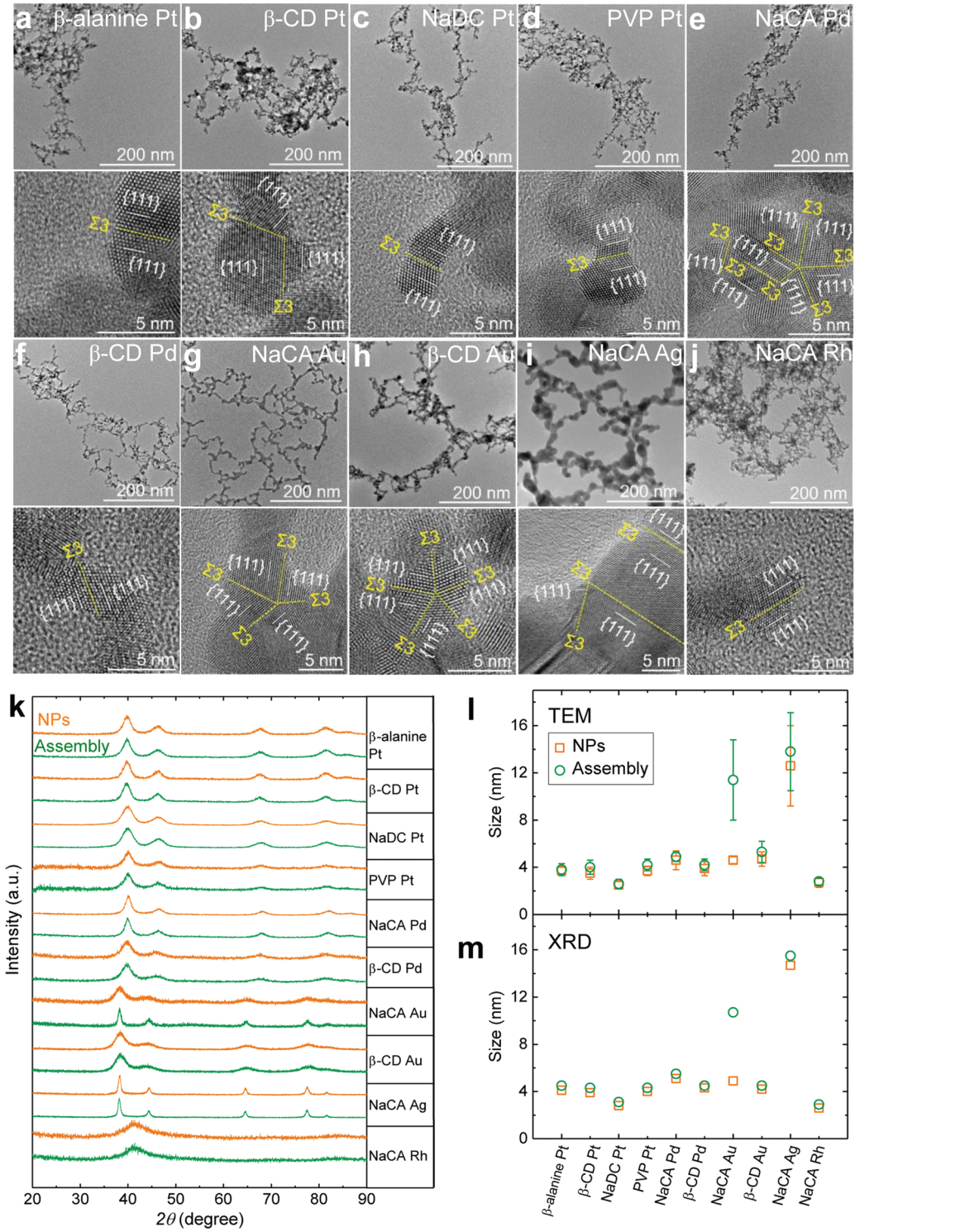

Figure 3. Synthesis of Σ3 (111) twin GB-rich noble metal NP assemblies. TEM and HRTEM images of a–d) Pt NP assemblies prepared from Pt NPs with various ligands, including *β*-alanine, *β*-cyclodextrin (*β*-CD), sodium deoxycholate (NaDC), and polyvinylpyrrolidone (PVP), e,f) Pd NP assemblies prepared from sodium citrate (NaCA)- and *β*-CD-capped Pd NPs, g,h) Au NP assemblies prepared from NaCA- and *β*-CD-capped Au NPs, i) Ag and j) Rh NP assemblies from their NaCA-capped NPs. k) XRD spectra of the NPs and their corresponding assemblies. l,m) The crystallite size comparison between the NPs and their assemblies based on their TEM images and XRD spectra. The size distribution was obtained by analyzing ≈100 NPs or crystallites.

they are joined at this planar interface forming a twin GB. For metals with low twin-fault energies, such as Au and Pd, high-energy grain boundaries are likely to form and then decompose to multiply twinned structures. Due to the low intrinsic stacking-fault energy, Ag NP assemblies tend to form stacking faults to release the strain.

2.5. Catalytic Hydrogen Sensing Application

After establishing the synthetic method and its scope, we continued exploring the reactivities of these twin GB-rich noble metal NP assemblies. We discovered the exceptional performance of GB-rich Pt NP assemblies toward catalytic hydrogen sensing. We found that the GB-rich Pt NP assemblies were highly active for catalytic hydrogen oxidation in air, enabling room temperature catalytic hydrogen sensing for the first time. The room temperature operating condition addressed the low cross-sensitivity issue of conventional catalytic sensors discussed in the introduction section.

Our sensors were prepared by drop-casting a mixture of Pt NP assembly powder and ethanol onto a commercial thermocouple, followed by drying in air (**Figure 4**a, inset). The sensor response is the temperature change (ΔT) of the catalyst-coated thermocouple upon exposure to H_2. Figure 4a shows that the sensor temperature rapidly increased from room temperature of ≈22 to ≈360 °C in ≈10 s, after being exposed to a stream of 4% H_2 in air (i.e., the lower explosive limit of H_2). Upon the removal of H_2, the sensor temperature quickly returned to room temperature within 10 s. ΔT decreases in response to stepwise decreasing H_2 concentrations (C_{H2}) from 4% to 0.05%, yielding a linear relationship between ΔT and C_{H2} at the logarithmic scale (Figure 4c). In contrast, when the same loading (≈1 mg) of other Pt catalysts was used to prepare a catalytic H_2 sensor, including Pt NPs before assembly, Pt NPs after ligand removal, commercial Pt black, and Pt powder, the sensor response is mostly negligible (<1 °C) even at C_{H2} = 4% (Figure 4b). Because the electrochemically active surface area of Pt NP assembly powder was 129 ± 25 cm^2 mg^{-1}, ≈60% lower than that of Pt NPs (322 ± 37 cm^2 mg^{-1}) and Pt black (144 ± 5 cm^2 mg^{-1}, Figure S17, Supporting Information), suggesting the high catalytic activity of Pt NP assembly originates from its unique structure.

The response and recovery times of Pt NP assembly sensor, defined as the time to reach 90% of the total signal, were ≈7 s at C_{H2} >1% and extended to ≈1 min at 0.05% (Figure 4d). Such negative dependence of response and recovery times on C_{H2} is common for H_2 sensors because low C_{H2} is associated with a slow reaction rate between H_2 and the sensing material.[43–45] The response time is still better than the performance of existing catalytic H_2 sensors on the market (≈10–30 s).[46,47] It is important to point out that the Pt NP assembly sensor can discriminate different H_2 concentrations in 1 s based on its transient temperature change (Figure S18, Supporting Information). Due to the self-heating effect of Pt NP assembly during catalytic H_2 sensing, the sensor is operational over a broad ambient temperature range from −30 to 80 °C and a humidity range from 0 to 98% (Figure 4e; Figure S19, Supporting Information). When C_{H2} >2%, the environmental temperature and humidity do not affect the sensor response, response, or recovery times.

Most impressively, our sensor exhibited low cross-sensitivity and anti-poisoning properties. To evaluate these two metrics accurately, we adopted the interference/cross-sensitivity test protocol developed by the DOE National Renewable Energy Laboratory (Figure S20, Supporting Information).[48] Figure 4f plots the percentage change of sensor temperature when exposed to 36 different interference gases, including CO, NO_2, SO_2, H_2S, NH_3, and various organic gas and vapors such as natural gas, hexane, benzene, formaldehyde, methanol, etc., in the absence and presence of 4% H_2 (see raw data in Figure S20, Supporting Information). None of the interference gases has caused more than a 10% change in the sensor response, which is incredible because commercial catalytic H_2 sensors suffer from severe cross-sensitivity to combustible gases and vapors (for example, the relative sensitivity for CH_4 and H_2 is ≈1).[47] After being exposed to these interference gases, the sensor always returned to the initial state and produced the same response to H_2 as the calibrated value (Figure S20, Supporting Information), indicating no irreversible poisoning effect. Furthermore, the Pt NP assembly sensor exhibited high long-term stability. The sensor response remained constant during a 281-h-long 288-test-cycles test (Figure 4g; Figure S21, Supporting Information). The relative standard deviation of sensor response was ≈1% for C_{H2} ≥1%. The variation in sensor response at a low C_{H2} of 0.05% is possibly due to the slight fluctuation of ambient temperature. Furthermore, Σ3 GBs are stable and present after long-term H_2 sensing cycle test (Figure S22, Supporting Information).

Because the sensor readout is temperature change, our H_2 sensors can be conveniently fabricated using any commercially available thermometers (Figure S23, Supporting Information), making the sensor inexpensive (as low as <$5 per unit) and easily miniaturized (size <2 mm). The sensor response is also reproducible and consistent among all the sensors built from different thermometers (Figure S24, Supporting Information). Furthermore, we built a portable and wireless gas sensing system prototype that can be loaded onto a commercial drone and demonstrated its practicality for H_2 leak detection (Figure S25 and Movies S1 and S2, Supporting Information).

2.6. The Reactivity at GB Sites

To confirm that the GB sites are responsible for the high catalytic activity, we correlated the GB-density of the NP assembly with its catalytic hydrogen oxidation activity as follows.

First, we synthesized Pt NP assemblies with different GB-densities by varying the electrode potential from −1.5 to −3 V during electrosynthesis. At high potentials, the fast bubble generation increases the flow, resulting in high connectivity between NPs and thus high GB density (a denser network of NP chains in **Figure 5**a–d). The electrode potential-dependent morphology evolution from a loose network to more compact one is because the flow increases the NP collision frequency, resulting in the "evening out" of growth probability between sites, which in turn accounts for the increasing degree of compactness of the aggregate.[49,50] For all samples, Σ3 (111) twin GBs are the

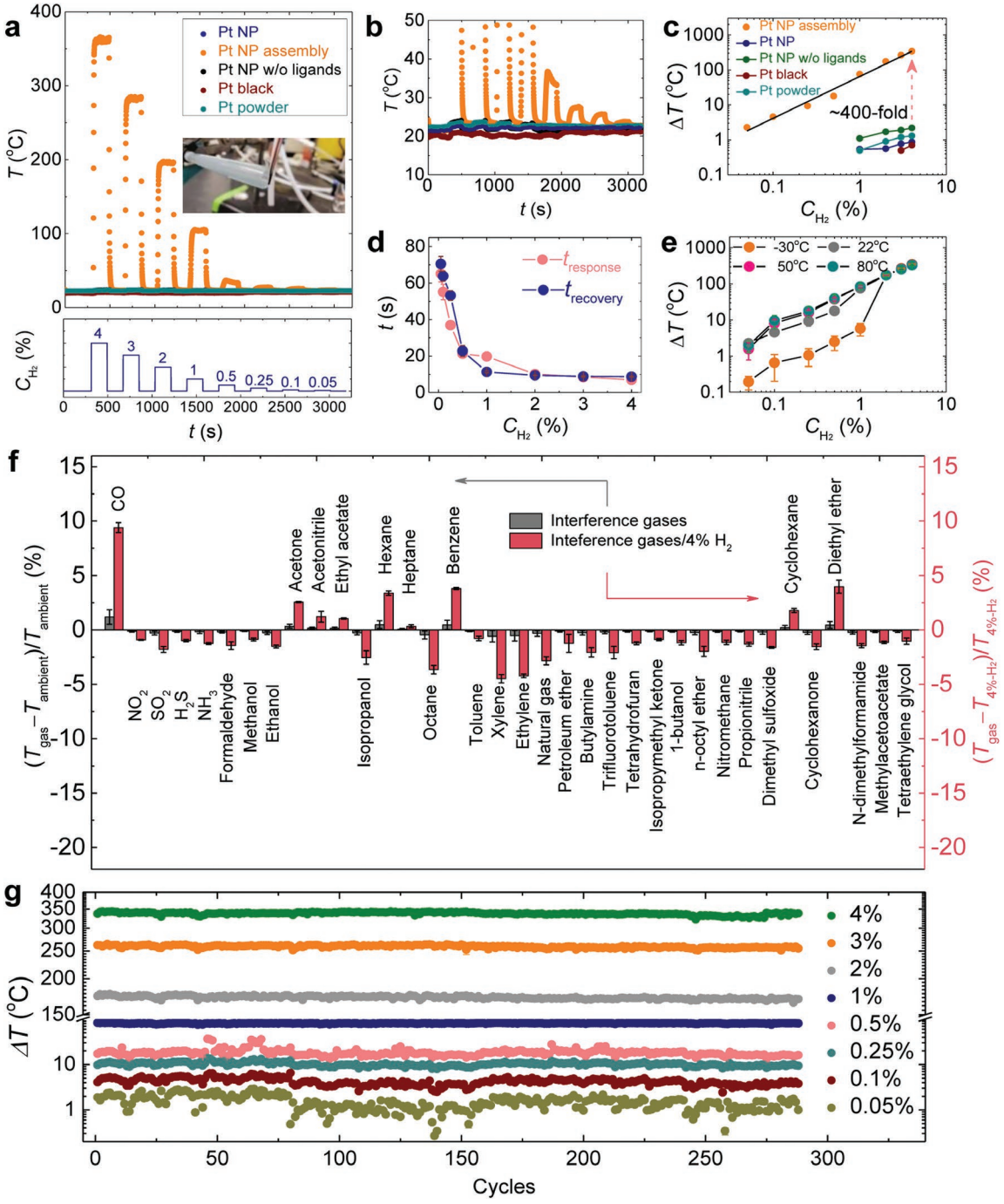

Figure 4. Catalytic hydrogen sensing performance of GB-rich Pt NP assembly at room temperature. a) Temperature readout (T) of the catalytic hydrogen sensors built using Pt NPs (blue dots), Pt NP assembly (orange dots), Pt NPs without ligands (green dots, see Figure S1, Supporting Information), commercial Pt black (red dots), and Pt powder (cyan dots) in response to stepwise decreasing H_2 concentrations (C_{H2}) from 4% to 0.05% in air at room temperature. The sensor temperature was recorded at 1 point per second. Insets of (a) are a photograph of a catalytic hydrogen sensor (a J-type thermocouple coated with Pt catalyst) and b) an expanded view of the temperature response curves. c) Sensor response ($\Delta T = T - T_{ambient}$, where $T_{ambient}$ is the ambient temperature) as a function of C_{H2} for Pt NP assembly (orange dots) and other Pt catalysts, showing ≈400-fold improvement over the sensor response using the Pt NP assembly catalyst. d) Response time ($t_{response}$) and recovery time ($t_{recovery}$) of Pt NP assembly sensor at various C_{H2}. e) Measured ΔT as a function of C_{H2} when the Pt NP assembly-based sensor was operated at an ambient temperature range from −30 to 80 °C. f) The percentage change of sensor response when exposed to 36 different interference gases in the absence (gray bars) and presence (red bars) of 4% H_2 in air. g) Stability of the Pt NP assembly-based hydrogen sensor during a 280-h-long 288-test-cycles test. In each cycle, was decreased from 4% to 0.05% stepwise, as in panel (a). The error bars are the standard deviations from three independent devices.

dominant GB type, the crystallite size and Pt oxidation state did not change during assembly (Figure 5e; Figure S26, Supporting Information), and surface citrate ligands were also completely removed (Figure S26, Supporting Information).

Assuming every NP attachment event forms one GB, we can estimate the GB surface density, defined as the ratio of total GB length to the exposed surface area ($l_{GB}/A_{assembly}$), from the surface area loss during NP assembly using the following equation (see details in Supporting Information):

$$\text{GB density} = \frac{l_{GB}}{A_{assembly}} = \frac{2A_{GB}/r}{A_{assembly}} = \frac{(A_{NP} - A_{assembly})r}{A_{assembly}} \quad (1)$$

where r is the average GB radius, A_{GB} is the GB area, and A_{NP} and $A_{assembly}$ are the total surface areas of NPs and their corresponding assembly, respectively. The value of r was determined by sizing 100 GBs from the HR-TEM images of NP assemblies (Figure S27, Supporting Information). A_{NP} and $A_{assembly}$ were measured by hydrogen adsorption/desorption using cyclic voltammetry (CV) under the same catalyst loading. The CVs in Figure 5f show the current associated with hydrogen adsorption/desorption (between –0.2 and 0.1 V) decreased with increasing synthesis potential, consistent with the TEM morphology of higher NP connectivity at higher potentials. We found that the GB density of NP assembly increased gradually from 636 μm^{-1} at –1.5 V to 1589 μm^{-1} at –3.0 V (Figure S28, Supporting Information). Note, because some NP attachments with perfect alignment form interface-free crystals,[26] the above equation results in a higher GB density than the actual one. However, this does not change the trend of GB densities calculated at different experimental conditions.

Next, we evaluated the catalytic hydrogen sensing performance of these NP assemblies with various GB surface densities. Figure 5g and Figure S29 (Supporting Information) shows that the sensor response (ΔT) increases with the GB density. Considering regular Pt sites do not catalyze hydrogen oxidation at room temperature (Figure 4c), the positive linear correlation between ΔT and the GB density in Figure 5h and Figure S30 (Supporting Information) clearly shows that the GB sites are responsible for the high catalytic activity.

2.7. Theoretical Calculations

Finally, we conducted DFT calculations to understand the origin of high catalytic H_2 oxidation activity at the GB sites. We built a Pt_{201} NP model with 201 Pt atoms and a Pt_{383} Σ3 (111) twin boundary model formed between two Pt_{201} NPs (Figure S31, Supporting Information). We first validated the twin boundary model by comparing theoretically calculated and experimentally measured strain fields at the GB sites. Figure 5i shows the DFT optimized structure that reveals that ≈2% tensile strain is present at the Σ3 GB along the direction normal to {111} planes. For Σ3 (111) GBs formed between two larger Pt NPs (e.g., Pt_{783} Σ3 (111) GB in Figure S32, Supporting Information), we observed a similar tensile strain at the GB region. These calculated strain values are lower than the experimentally observed high strain of 7% by STEM (Figure S33, Supporting Information), but still should be sufficiently accurate for qualitatively studying the catalytic H_2 reaction mechanism. The difference between calculated and experimental strain values is possibly due to the long-chain network in Pt NP assembly in contrast to the (111) twin boundary of two particles in the DFT simulation (Figure 5i).

Next, we performed DFT calculations on the two possible hydrogen oxidation mechanisms (i.e., associative and dissociative pathways) using the Pt_{383} GB model.[51] We compared the results from the GB model with Pt (111) slabs and Pt_{201} NP models (Figure S34–S36, Supporting Information). DFT results in Figure 5j and Figures S36 and S37 (Supporting Information) show that the associative pathway dominates for Pt (111) slabs and Pt_{201} NP (111) facet, owing to its lower energy barrier at the rate-determining step (i.e., OOH* formation, 0.38–0.42 eV, Table S1, Supporting Information) than that of the dissociative pathway (O_2* dissociation: 0.54–0.72 eV or OH* formation: 0.75–1.02 eV, Table S2, Supporting Information). Furthermore, we found a substantial enhancement of the associative H_2 oxidation rate due to the tensile strain on Pt (111) slabs (green circles in Figure 5j). Such tensile strain-induced enhancement was also observed, but less pronounced, for the Σ3 GB region with respect to isolated Pt NP (green pentagon vs triangle in Figure 5j).

More excitingly, we discovered that the activation barrier of O_2* dissociation at the Σ3 GB was extensively reduced to merely 0.008 eV (Table S2 and Figures S36 and S37, Supporting Information), making the dissociative pathway more favorable in the GB region. Besides, the activation barrier for the rate-determining step in the dissociative pathway (i.e., OH* formation) was lowered from 1.02 eV on Pt_{201} NP (111) facet to 0.60 eV at the Σ3 GB region (Figure 5k), accelerating H_2 oxidation through the dissociative pathway by 12 orders of magnitude relative to that on the (111) facet of Pt NP (orange pentagon vs orange triangle, Figure 5j). Also, it is worth noting that the decrease in reaction rate with tensile strain was found in a slab model for the dissociative pathway, which seems contradictory to the improved rate at the GB region with tensile strain. It is possibly because the slab model has quite a different local environment from the GB model. Taken together, the DFT results suggest that H_2 oxidation via the associative and dissociative pathways is both enhanced at the Σ3 GBs. However, the dissociative pathway is dominant due to the remarkably lowered activation barriers of O_2* dissociation and OH* formation at the Σ3 GB region.

3. Conclusion

In summary, we developed a facile and scalable method for synthesizing Σ3 (111) twin GB-rich noble metal NP assemblies from Pt, Pd, Au, Ag, and Rh NPs with various ligands, including sodium citrate, β-alanine, β-cyclodextrin, sodium deoxycholate, and polyvinylpyrrolidone. Our method utilizes the electrogenerated H_2 and localized high pH at the cathode to remove the ligands on NPs and promote the random collisions of NPs in solution. The colliding NPs are joined mainly at the {111} plane via OA, forming the Σ3 (111) twin GBs. Structural characterization reveals that the NP assemblies have similar crystallite sizes as their NP precursors. For Pt NP assemblies, there is no global lattice strain but higher local structural disorder or microstrain at the Σ3 (111) twin GBs, compared to Pt NPs.

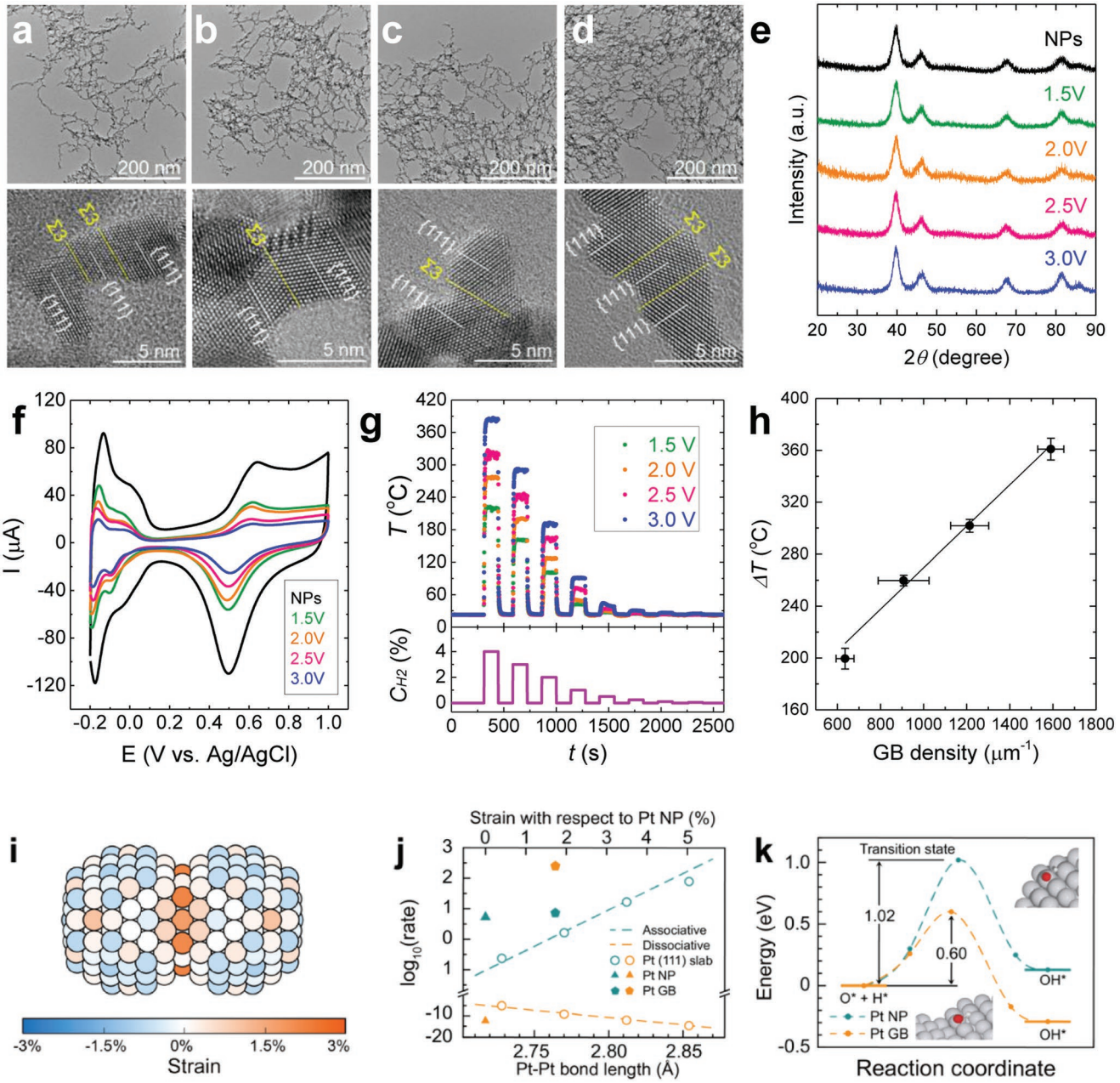

Figure 5. The reactivity at Pt Σ3 (111) twin GB sites. TEM and HRTEM images of a–d) Pt NP assemblies with different connectivities synthesized at various potentials of −1.5, −2.0, −2.5, and −3.0 V, respectively. e) XRD spectra of these assemblies and their NP precursor show no crystallite size change. f) Electrochemical surface area (ECSA) measurements of NPs and assemblies with the same catalyst loading of 4 μg at scan rate = 50 mV s^{-1}. g) Temperature readout (T) of Pt NP assemblies in response to stepwise decreasing H_2 concentrations (C_{H2}) from 4% to 0.05% in air at room temperature. h) Correlation between temperature variation towards 4% C_{H2} and GB density. GB densities were calculated from the loss of ECSA during NP assembly and the average TEM GB length (see Supporting Information). i) Calculated strain distribution in a Pt_{383} Σ3 (111) twin boundary model (formed between two Pt_{201} NPs). The subscripts of the notations show the total number of Pt atoms in each model. The strain values are referenced to the (111) facet of an isolated Pt_{201} NP. j) Calculated H_2 oxidation rates on Pt (111) slabs with different Pt—Pt bond lengths (circles), isolated Pt_{201} NP (111) facet (triangles), and the Σ3 (111) GB (pentagons). The associative and dissociative reaction pathways are marked green and orange, respectively. k) Calculated minimum energy path of the rate-determining step in the dissociative pathway: O* + H* → OH*, on the Pt_{201} NP (111) facet and the Pt_{383} Σ3 (111) GB. Insets show the corresponding transition states on NP and GB. The error bars are the standard deviations from three independent samples or devices.

We also discovered the ultrahigh activity of Pt NP assemblies for catalytic hydrogen oxidation in air, enabling room temperature catalytic hydrogen sensing for the first time. Our sensor shows low cross-sensitivity when exposed to 36 different interference gases, including CO, NO_2, SO_2, H_2S, NH_3, and various organic gas and vapors such as natural gas, hexane, benzene, formaldehyde, and methanol, addressing the most significant limitation of existing catalytic H_2 sensors. Our sensor also

exhibits fast response and recovery (≈7 s) and high long-term stability, evidenced by no signal drifting during a 281-h-long 288-test-cycles test. Because the sensor readout is temperature, our sensors can be conveniently prepared from any commercial thermometers at a cost as low as <$5 per unit and are easily miniaturized (size <2 mm).

With the help of advanced structural characterization techniques and theoretical calculations, we revealed that the high catalytic activity of Σ3 GB-rich Pt NP assembly should arise from the unique activity at the GB region, which facilitates adsorbed O_2 dissociation and drastically accelerates the hydrogen oxidation reaction via the dissociative pathway.

Given the recently discovered high activities of GBs for other catalytic reactions such as CO_2 electroreduction and methane activation, our synthetic approach will be also powerful for studying the GB activity for these reactions because it provides well-defined Σ3 (111) twin GBs as well as convenient control over the GB density for establishing the structure-activity relationship, and offers a unique opportunity for many other important applications in the future.[52,53]

Supporting Information

Supporting Information is available from the Wiley Online Library or from the author.

Acknowledgements

X.G., S.L., and J.H. contributed equally to this work. This research was supported by the U.S. Department of Energy (DOE), Office of Science, Office of Basic Energy Sciences, (BES) under Award # 78705 (material synthesis and evaluation) and Early Career Research program under Award KC0203020:67037 (TEM characterization), by the National Science Foundation (NSF) under Award # CHE-1943737 (preliminary studies) and # DMR-1654140 (XAS studies), and by the National Natural Science Foundation of China (NSFC) under grant No. 22103047 and startup funds from Tsinghua University (computational studies). In addition, this research used the resources of the Advanced Photon Source, a DOE Office of Science User Facility operated for the DOE Office of Science by Argonne National Laboratory under Contract No. DE-AC02-06CH11357 and the TEM facility in the William R. Wiley Environmental Molecular Sciences Laboratory (EMSL), a national scientific user facility sponsored by the DOE Office of Biological and Environmental Research and located at Pacific Northwest National Laboratory (PNNL). PNNL is a multiprogram national laboratory operated for the DOE by Battelle under Contract No. DE-AC05-76RL01830. The authors also thank Drs. Hua Zhou and Xiaobing Zuo at Argonne National Laboratory for performing the Small-angle X-ray scattering measurements.

Conflict of Interest

A U.S. provisional patent application (no. 63/278,451) based on the technology described in this work was filed on 11 Nov 2021 by L.L. and X.G. at Wayne State University.

Data Availability Statement

The data that support the findings of this study are available in the supplementary material of this article.

Keywords

catalyses, electrosyntheses, grain boundaries, hydrogen sensors, nanoparticle assemblies, noble metals

Received: April 13, 2022
Revised: May 23, 2022
Published online:

[1] T. Watanabe, *J. Mater. Sci.* **2011**, *46*, 4095.
[2] R. G. Mariano, K. McKelvey, H. S. White, M. W. Kanan, *Science* **2017**, *358*, 1187.
[3] X. Feng, K. Jiang, S. Fan, M. W. Kanan, *J. Am. Chem. Soc.* **2015**, *137*, 4606.
[4] R. G. Mariano, M. Kang, O. J. Wahab, I. J. McPherson, J. A. Rabinowitz, P. R. Unwin, M. W. Kanan, *Nat. Mater.* **2021**, *20*, 1000.
[5] X. Feng, K. Jiang, S. Fan, M. W. Kanan, *ACS Cent. Sci.* **2016**, *2*, 169.
[6] A. Verdaguer-Casadevall, C. W. Li, T. P. Johansson, S. B. Scott, J. T. McKeown, M. Kumar, I. E. L. Stephens, M. W. Kanan, I. Chorkendorff, *J. Am. Chem. Soc.* **2015**, *137*, 9808.
[7] W. Huang, A. C. Johnston-Peck, T. Wolter, W. D. Yang, L. Xu, J. Oh, B. A. Reeves, C. Zhou, M. E. Holtz, A. A. Herzing, A. M. Lindenberg, M. Mavrikakis, M. Cargnello, *Science* **2021**, *373*, 1518.
[8] J.-Q. Wang, C. Xi, M. Wang, L. Shang, J. Mao, C.-K. Dong, H. Liu, S. A. Kulinich, X.-W. Du, *ACS Catal.* **2020**, *10*, 12575.
[9] Z. Li, J.-Y. Fu, Y. Feng, C.-K. Dong, H. Liu, X.-W. Du, *Nat. Catal.* **2019**, *2*, 1107.
[10] X.-J. Liu, X. Yin, Y.-D. Sun, F.-J. Yu, X.-W. Gao, L.-J. Fu, Y.-P. Wu, Y.-H. Chen, *Nanoscale* **2020**, *12*, 5368.
[11] H. You, F. Gao, C. Wang, J. Li, K. Zhang, Y. Zhang, Y. Du, *Nanoscale* **2021**, *13*, 17939.
[12] Y. Nagaoka, M. Suda, I. Yoon, N. Chen, H. Yang, Y. Liu, B. A. Anzures, S. W. Parman, Z. Wang, M. Grünwald, H. M. Yamamoto, O. Chen, *Chem* **2021**, *7*, 509.
[13] V. V. Bulatov, B. W. Reed, M. Kumar, *Acta Mater.* **2014**, *65*, 161.
[14] L. Boon-Brett, J. Bousek, P. Moretto, *Int. J. Hydrogen Energy* **2009**, *34*, 562.
[15] L. Boon-Brett, J. Bousek, G. Black, P. Moretto, P. Castello, T. Hübert, U. Banach, *Int. J. Hydrogen Energy* **2010**, *35*, 373.
[16] V. Palmisano, E. Weidner, L. Boon-Brett, C. Bonato, F. Harskamp, P. Moretto, M. B. Post, R. Burgess, C. Rivkin, W. J. Buttner, *Int. J. Hydrogen Energy* **2015**, *40*, 11740.
[17] T. Hübert, L. Boon-Brett, G. Black, U. Banach, *Sens. Actuators B: Chem.* **2011**, *157*, 329.
[18] E.-B. Lee, I.-S. Hwang, J.-H. Cha, H.-J. Lee, W.-B. Lee, J. J. Pak, J.-H. Lee, B.-K. Ju, *Sens. Actuators B: Chem.* **2011**, *153*, 392.
[19] A. Harley-Trochimczyk, T. Pham, J. Chang, E. Chen, M. A. Worsley, A. Zettl, W. Mickelson, R. Maboudian, *Adv. Funct. Mater.* **2016**, *26*, 433.
[20] D. Del Orbe Henriquez, I. Cho, H. Yang, J. Choi, M. Kang, K. S. Chang, C. B. Jeong, S. W. Han, I. Park, *ACS Appl. Nano Mater.* **2020**, *4*, 7.
[21] X. Liu, H. Dong, S. Xia, *Micro Nano Lett* **2013**, *8*, 668.
[22] R. E. Cavicchi, G. E. Poirier, N. H. Tea, M. Afridi, D. Berning, A. Hefner, J. Suehle, M. Gaitan, S. Semancik, C. Montgomery, *Sens. Actuators B: Chem.* **2004**, *97*, 22.
[23] A. Harley-Trochimczyk, J. Chang, Q. Zhou, J. Dong, T. Pham, M. A. Worsley, R. Maboudian, A. Zettl, W. Mickelson, *Sens. Actuators B: Chem.* **2015**, *206*, 399.
[24] S. Jungblut, J.-O. Joswig, A. Eychmüller, *Phys. Chem. Chem. Phys.* **2019**, *21*, 5723.
[25] J. Buffle, G. G. Leppard, *Environ. Sci. Technol.* **1995**, *29*, 2169.
[26] M. Song, G. Zhou, N. Lu, J. Lee, E. Nakouzi, H. Wang, D. Li, *Science* **2020**, *367*, 40.

[27] H. Grimmer, W. Bollmann, D. H. Warrington, *Acta Crystallogr. A* **1974**, *30*, 197.
[28] C. Zhu, S. Liang, E. Song, Y. Zhou, W. Wang, F. Shan, Y. Shi, C. Hao, K. Yin, T. Zhang, J. Liu, H. Zheng, L. Sun, *Nat. Commun.* **2018**, *9*, 421.
[29] R. L. Penn, J. F. Banfield, *Science* **1998**, *281*, 969.
[30] F. D. Vila, J. J. Rehr, H. H. Rossner, H. J. Krappe, *Phys. Rev. B* **2007**, *76*, 014301.
[31] R. Chattot, O. Le Bacq, V. Beermann, S. Kühl, J. Herranz, S. Henning, L. Kühn, T. Asset, L. Guétaz, G. Renou, J. Drnec, P. Bordet, A. Pasturel, A. Eychmüller, T. J. Schmidt, P. Strasser, L. Dubau, F. Maillard, *Nat. Mater.* **2018**, *17*, 827.
[32] T. Ungár, *Scr. Mater.* **2004**, *51*, 777.
[33] K. Venkateswarlu, A. Chandra Bose, N. Rameshbabu, *Phys. B: Condens. Matter* **2010**, *405*, 4256.
[34] S. Zhou, M. Zhao, T.-H. Yang, Y. Xia, *Mater. Today* **2019**, *22*, 108.
[35] N. M. Rosengaard, H. L. Skriver, *Phys Rev B Condens Matter* **1993**, *47*, 12865.
[36] M. J. Yacamán, J. A. Ascencio, H. B. Liu, J. Gardea-Torresdey, *Journal of Vacuum Science & Technology B: Microelectronics and Nanometer Structures Processing, Measurement, and Phenomena* **2001**, *19*, 1091.
[37] M. Song, Z. Wu, N. Lu, D. Li, *Chem. Mater.* **2019**, *31*, 842.
[38] F. T. L. Muniz, M. R. Miranda, C. Morilla dos Santos, J. M. Sasaki, *Acta Crystallographica Section A: Foundations and Advances* **2016**, *72*, 385.
[39] U. Holzwarth, N. Gibson, *Nat. Nanotechnol.* **2011**, *6*, 534.
[40] G. Yang, S. A. Akhade, X. Chen, Y. Liu, M.-S. Lee, V.-A. Glezakou, R. Rousseau, J. A. Lercher, *Angew. Chem., Int. Ed.* **2019**, *58*, 3527.
[41] I. S. P. Savizi, M. J. Janik, *Electrochim. Acta* **2011**, *56*, 3996.
[42] F. Matter, A. L. Luna, M. Niederberger, *Nano Today* **2020**, *30*, 100827.
[43] W.-T. Koo, H.-J. Cho, D.-H. Kim, Y. H. Kim, H. Shin, R. M. Penner, I.-D. Kim, *ACS Nano* **2020**, *14*, 14284.
[44] R. M. Penner, *Acc. Chem. Res.* **2017**, *50*, 1902.
[45] I. Darmadi, F. A. A. Nugroho, C. Langhammer, *ACS Sens.* **2020**, *5*, 3306.
[46] M. Krawczyk, J. Namiesnik, *J. Autom. Methods Manag. Chem.* **2003**, *25*, 115.
[47] C. Batchelor-McAuley, J. Ellison, K. Tschulik, P. L. Hurst, R. Boldt, R. G. Compton, *Analyst* **2015**, *140*, 5048.
[48] L. J. Loh, G. C. Bandara, G. L. Weber, V. T. Remcho, *Analyst* **2015**, *140*, 5501.
[49] J. A. Kaandorp, C. P. Lowe, D. Frenkel, P. M. A. Sloot, *Phys. Rev. Lett.* **1996**, *77*, 2328.
[50] R. K. Chakraborti, K. H. Gardner, J. F. Atkinson, J. E. Van Benschoten, *Water Res.* **2003**, *37*, 873.
[51] L. Qi, J. Yu, J. Li, *J. Chem. Phys.* **2006**, *125*, 054701.
[52] J. Li, C. Wang, H. Shang, Y. Wang, H. You, H. Xu, Y. Du, *Chem. Eng. J.* **2021**, *424*, 130319.
[53] C. Wang, H. Shang, J. Li, Y. Wang, H. Xu, C. Wang, J. Guo, Y. Du, *Chem. Eng. J.* **2021**, *420*, 129805.